Physica Medica 66 (2019) 36–44

Contents lists available at ScienceDirect

Physica Medica

journal homepage: www.elsevier.com/locate/ejmp

Technical note

Improved Monte Carlo clinical electron beam modelling

K.N. Sachse*, F.C.P. du Plessis*

Department of Medical Physics, Faculty of Health Sciences, University of the Free State, P.O. Box 339, Bloemfontein 9300, South Africa

ARTICLE INFO

Keywords:
Electron modelling
Monte Carlo
EGSnrc
BEAMnrc
DOSXYZnrc
Energy spectrum
Focal spot

ABSTRACT

Purpose: An EGSnrc based electron model was developed and validated for an Elekta Synergy® 160-leaf Agility™ linear accelerator. It was able to reproduce measured central axis (CAX) percentage depth dose (PDD) curves and off-axis profiles (OAPs) within 2%/2 mm, and relative output factors (ROFs) within 3%.

Methods: BEAMnrc component modules were used to model the accelerator accurately according to vendor supplied specifications. The electron beam focal spot size and input energy spectrum were determined through their effects on electron CAX PDDs and OAPs as benchmarked against water tank data. Phase space files were used as source input in DOSXYZnrc water phantom simulations. Dose distributions were calculated for six electron nominal energies, 11 field sizes and two source-to-surface distances.

Results: The full width at half maximum of the focal spot (assuming a Gaussian intensity distribution) was determined to be 1.50 mm. An asymmetrical input electron energy spectrum with a low-energy tail produced good agreement with measured data and solved the match in the build-up (BU) region for all electron energies used in this study.

Conclusions: The improved input electron spectra for the electron model could predict dose distributions within 2%/2 mm of measured data. The model's success is embedded in the asymmetrical energy spectrum which provided a valuable free parameter which, by fine adjustment, improved the match in the BU region of dose distributions. Furthermore, focal spot parameters could be determined by means of iterative simulations.

1. Introduction

Clinical electron beams are used in the treatment of intact breast lesions, chest wall irradiation for breast cancer, skin cancers, total scalp treatments, cancer of the parotid, nose, eye/orbit and eyelid, retinoblastomas, craniospinal irradiation, boost treatments (breast) and applications in Intraoperative Radiotherapy [1,2].

Electron beam treatment planning utilizing Monte Carlo (MC) methods have been shown to be the most accurate in both homogeneous and inhomogeneous media when compared to measurements, and is seen as the golden standard for treatment planning. Clinical electron beams have been modelled by several authors using the EGSnrc code system where an accuracy of 2%/2 mm have been attained. [3–14] Some approaches included the use of beam characterization models (single- or multiple sources), whereas other approaches included the complete modelling of the linear accelerator (linac) head using BEAMnrc (or earlier versions) to produce phase space files for subsequent dose calculations. Amongst these studies the incident electron energy spectrum was most commonly characterized by either a monoenergetic spectrum [14–18] or a Gaussian poly-energetic spectrum [19–25,27], though deconvolution methods have also been used to determine the energy spectrum [26,28–30]. From some of these studies it is evident that dose discrepancies larger than 2%/2 mm in the build-up (BU) region still exist. This was also recognized by the American Association of Physicists in Medicine (AAPM) [4] and was evident in the preliminary stages of this study. Using these energy spectra, it can be very challenging to only alter the dose in the BU region without causing significant changes to the rest of the central axis percentage depth dose (CAX PDD) curve. Different electron energy spectra and their influence on absorbed dose distributions have been investigated before [19], however none investigated a spectrum such as that used within this study. For this reason, this study investigated a poly-energetic input electron energy spectrum which shows its potential to be the solution to the observed BU dose discrepancies. This spectrum reflects the exit electron energy spectra as seen after the final collimation of electron beams [7,14,16,18,25,31] and includes a parameter which by minor adjustments can bring about changes in the BU region alone.

The objective for this study was to develop an accurate MC electron beam model for an Elekta Synergy® Agility™ linear accelerator using the EGSnrc/BEAMnrc code package. It was required that our model must be able to reproduce measured CAX PDD curves and off-axis profiles

* Corresponding authors.
E-mail addresses: 2012026247@ufs4life.ac.za (K.N. Sachse), DuPlessisFCP@ufs.ac.za (F.C.P. du Plessis).

https://doi.org/10.1016/j.ejmp.2019.09.073
Received 20 February 2019; Received in revised form 30 July 2019; Accepted 7 September 2019
Available online 21 September 2019

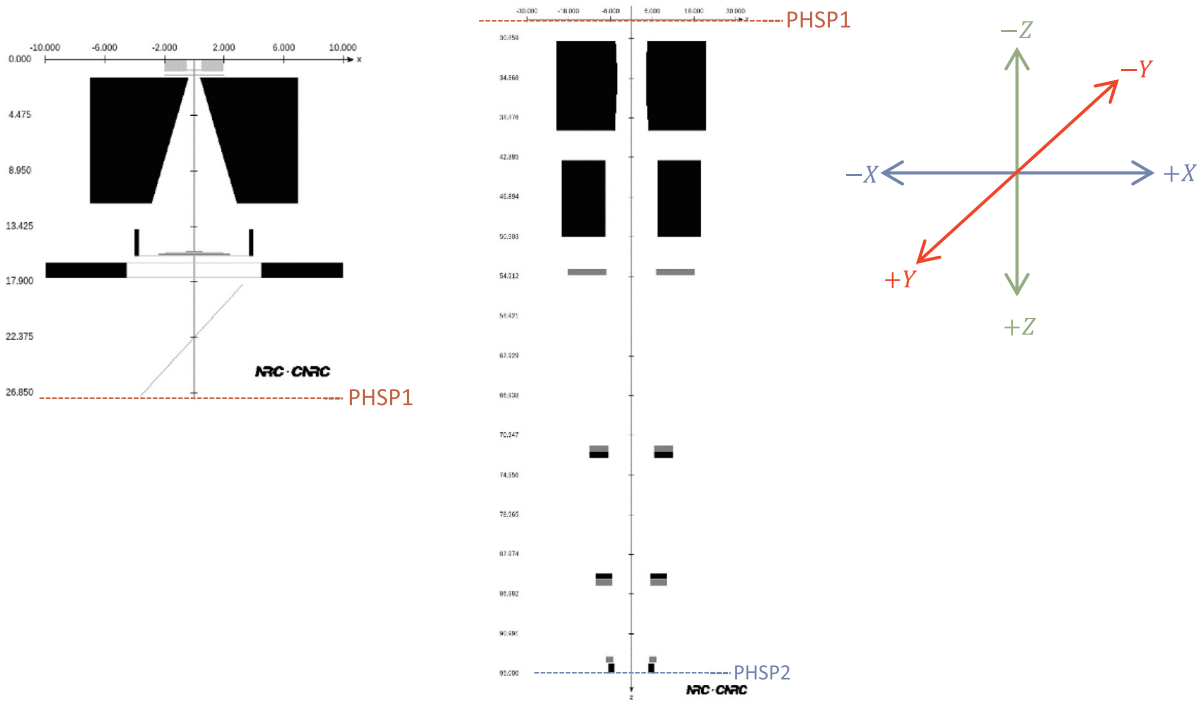

Fig 1. Upper/Common (left) and lower/specific (middle) BEAMnrc model of an Elekta Synergy® Agility™ linac. The phase space (PHSP1) file produced in the upper model is used as source input in the lower model, whereas the PHSP2 produced by the lower model is used as source input in DOSXYZnrc for subsequent dose calculations. The beam coordinate system used throughout this study is shown on the right, with X corresponding to the crossline direction and Y to the inline direction. The Z-axis is along the beam's axis when the gantry is on 0 degrees.

(OAPs) within 2%/2 mm, and relative output factors (ROFs) within at least 3%. Six clinical electron energies (4, 6, 8, 10, 12 and 15 MeV), 11 field sizes (2 × 2, 3 × 3, 6 × 6, 10 × 10, 14 × 14, 20 × 20, 6 × 10, 6 × 14, 8 × 16, 10 × 20 cm^2 and a 4 cm diameter circular field) and two source-to-surface distances (SSDs) (95 and 100 cm) were benchmarked against measured data.

2. Materials and methods

2.1. Linac head modelling

EGSnrc/BEAMnrc [32,33] was used to model each linac component using component modules (CMs) and to simulate electron beam transport through them. Detailed schematics of each component was obtained from the vendor. The CM Conestak was used to model the exit window, primary scattering foil, primary collimator and the screen. Similarly, the CM Flatfilt, Chamber, Mirror, MLCQ, Applicat and Pyramids were chosen to model the secondary scattering foils, dual ionization chamber, light-field mirror, Multi-leaf Collimator (MLC), Jaw, electron applicators and open field inserts, respectively, as shown in Fig. 1. For each applicator-electron energy combination, MLC and Jaw positions (defined at isocentre) are predetermined by the vendor which were determined using Elekta's customer acceptance tool, iCOM CAT (see Supplementary figure 1) [34].

In the light of simulation efficiency, re-usage of phase space files was implemented. An upper/common model was developed for each electron nominal energy, whereas a lower/specific model was developed for each field size, as shown in Fig. 1. The specific model uses the PHSP1 file produced by the common model as source input, and in turn produces a PHSP2 file at an SSD of 95 cm.

2.2. Modelling of initial beam properties

The initial electron beam's focal spot (size and shape) and energy spectrum details are not vendor-supplied, therefore methods had to be established to determine these properties. BEAMnrc source option 19 was chosen to model the radiation source [33]. This models the incident initial electron beam with a Gaussian intensity distribution (circular or elliptical) with its width defined in terms of the full width at half maximum ($FWHM_X$ and $FWHM_Y$). In addition, the incident energy spectrum is modelled using either a monoenergetic or a poly-energetic spectrum.

2.3. Focal spot: size and shape

Huang et al. [35] measured the focal spot very accurately using a slit camera composed of alternating lead and paper sheets. However, in this study the size of the focal spot was determined through iterative simulations. Twelve sources with FWHMs ranging from 0.5 mm to 10.0 mm were simulated for a 10 × 10 cm^2, 4 MeV electron beam at 95 cm SSD, and the effect on the CAX PDD and OAPs were investigated from which the FWHM that complied best with measured were determined. The shape of the focal spot was assumed to be circular given the radial symmetry of secondary scattering foils [36].

2.4. Incident energy spectrum: Gaussian and Lévy

While it is simple to characterize the incident electron beam with a monoenergetic spectrum, this only provides a single adjustable parameter; the peak energy. Since it is the energy spectrum that is primarily responsible for the match of simulated PDD data with measured data, a 'single parameter regime' is often not adequate to achieve satisfactory dose distribution comparisons. A Gaussian energy spectrum is the conventional way to model the incident electron energy spectrum, which is dependent on a peak energy, FWHM, and lower- and higher-energy cut-offs.

In addition to an incident Gaussian electron energy spectrum, we investigated an experimental energy spectrum to better the match with

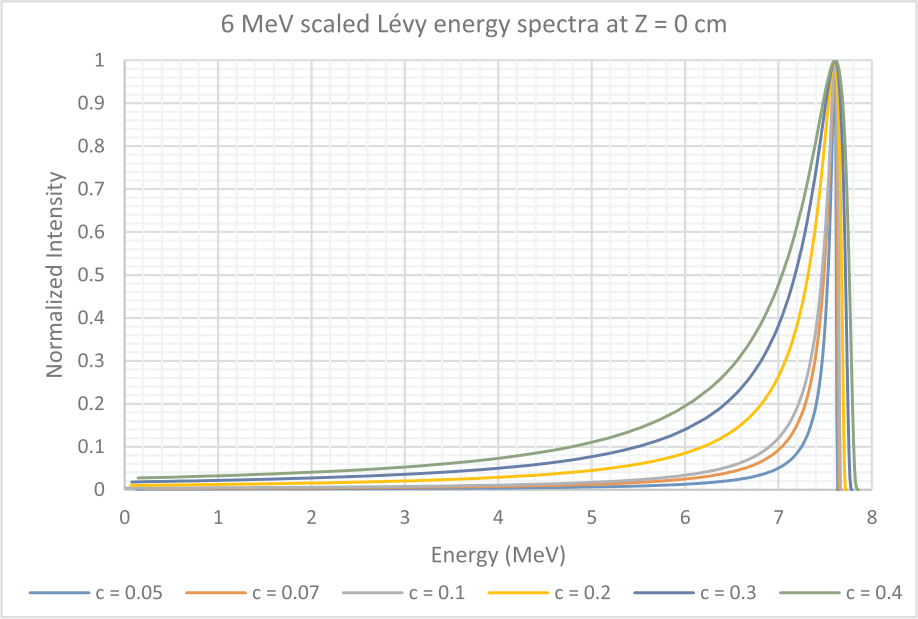

Fig 2. 6 MeV Lévy energy spectra as defined at Z = 0 cm with different scaling parameters ranging from 0.05 to 0.4. All spectra have a most probable electron energy of 7.605 MeV. The peak energy is determined iteratively by choosing the value that produces the best fit with the measured R_{50}. It is shown later on that the influence of the scaling parameter on R_{50} is extremely small. The maximum energy is mathematically determined by Eq. (1).

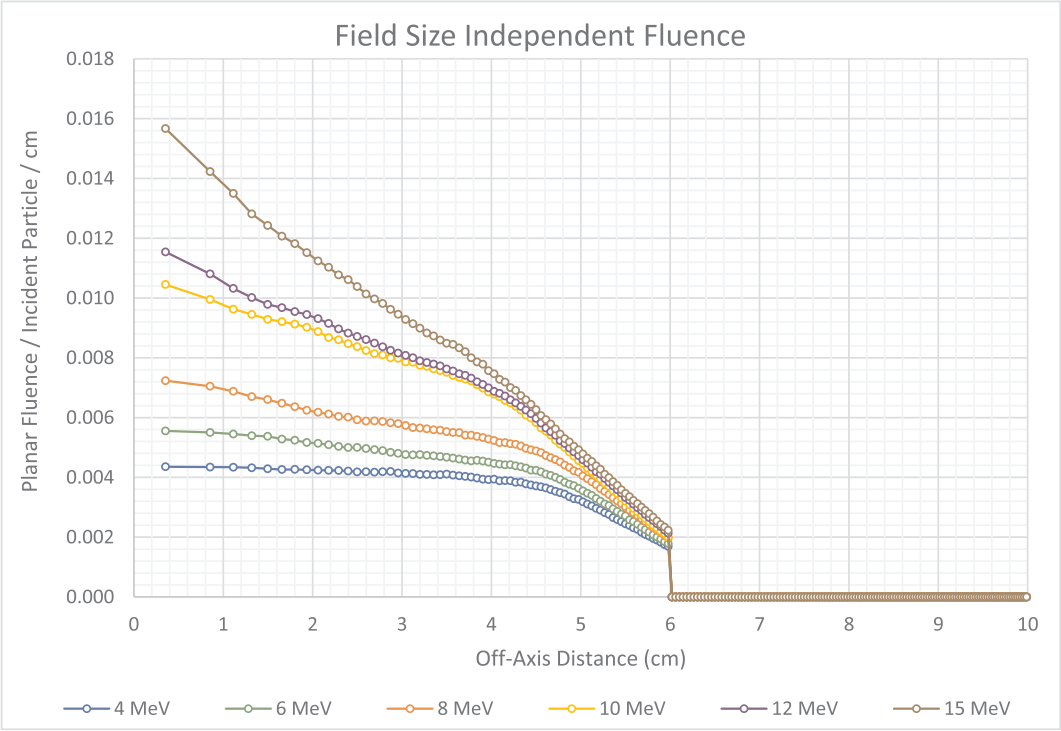

Fig 3. The field size independent total fluence for electron energies 4–15 MeV at the level of PHSP1. Plots were extracted using BEAMDP.

measured BU PDD data. This involves the modelling of a Landau distribution [37] according to a special case $f_L(E; \mu, c)$ in Paul Lévy's family of alpha-stable distributions [38], adapting it to the case of an energy spectrum. That is,

$$f_L(E; \mu, c) = A\frac{e^{-\frac{c}{2(E-\mu)}}}{(E-\mu)^{\frac{3}{2}}}; \text{with} f_L \in [\mu, \infty] \quad (1)$$

where μ and c are location and scaling parameters, respectively, E is the electron energy and A is a normalization constant. With the location parameter $\mu = 0$, the spectrum is valid for any positive energy. The spectrum is first constructed using energy values as input which produces a positive-skew distribution. This is then reflected about the Y-axis to produce a negative-skew distribution following a shift towards the relevant most probable energy (mode), producing a distribution as shown in Fig. 2.

Fig. 2 shows six different initial ($Z = 0$ cm) Lévy energy spectra for a 6 MeV electron beam. Spectra were constructed with a most probable electron energy of 7.605 MeV with scaling parameters of $c_1 = 0.05$, $c_2 = 0.07$, $c_3 = 0.1$, $c_4 = 0.2$, $c_5 = 0.3$ and $c_6 = 0.4$. The width

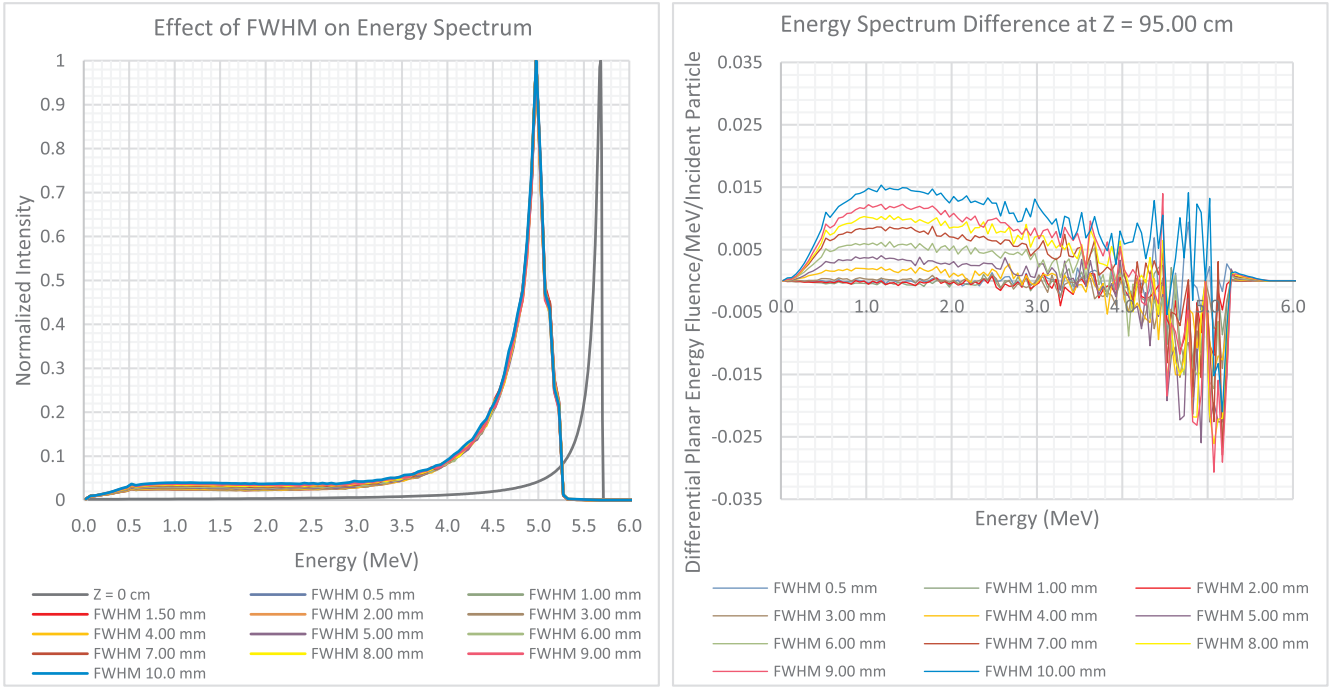

Fig 4. The effect of different focal spot FWHM on the energy spectrum at an SSD of 95 cm for a 10 × 10 cm^2, 4 MeV electron beam characterized by a Lévy energy spectrum at Z = 0 cm with a most probable energy of 5.685 MeV and a scaling parameter of 0.05. Left: The spectrum at Z = 0 cm (solid black line) and at Z = 95 cm (FWHM 0.5 mm to 10 mm). Right: The difference in the energy spectrum at Z = 95 cm brought about by different focal spot FWHM using the 1.5 mm FWHM as reference.

of the energy spectra increases with an increase in scaling parameter along with an increase in the lower energy tail.

Benchmarking of the model entails firstly matching the depth of maximum dose and R_{50}, along with the dose gradient, which are mostly dependent on the peak energy of the spectrum. A spatial misalignment in the dose fall-off region may be solved by adjusting the primary scattering foil thickness, which will also influence the dose in the BU region. The BU dose can be altered by making small adjustments to the scaling parameter of the energy spectrum which will minimally affect the dose beyond the maximum dose. Though the dose gradient is also sensitive to the width of the energy spectrum, the small alterations to be made in the scaling parameter would not significantly alter the dose gradient. A field size of 10 × 10 cm^2 was used as the initial field for fine tuning to ensure that scatter equilibrium is present on the CAX for all electron energies.

2.5. Monte Carlo transport parameters

The number of histories were determined prior to each simulation to obtain at most 1% variance, which ranged from 1.0 × 10^9 and 2 × 10^9 depending on the electron energy and field size. The field size independent fluences (at the level of PHSP1) for each electron energy are given in Fig. 3. Recycling of histories was implemented for DOSXYZnrc simulations. Bremsstrahlung splitting was implemented with a splitting number of 200, though this is of more importance in photon simulations. No bremsstrahlung cross-section enhancement, electron/photon splitting, electron range rejection or photon forcing was enabled. The global electron and photon energy cut-off parameters were set to 0.7 MeV and 0.01 MeV, respectively.

The maximum electron step length was the default value in the EXACT boundary crossing algorithm and PRESTA-II was the selected electron step algorithm. The maximum fractional energy loss per electron step was 0.25. The skin_depth_for_BCA parameter was set to 3 elastic mean free paths when broad electron fields were simulated and increased to 50 for small fields [39]. Spin effects were turned on as well as electron impact ionizations. The Koch and Motz equation was used for sampling of Bremsstrahlung angles, and Bethe-Heitler cross-sections was used for Bremsstrahlung and pair production sampling. Bound Compton scattering was turned on as well as photoelectron angular sampling. Atomic relaxations following a Compton and/or photoelectric event was simulated. All photon cross sections were based on the cross-sectional data from the ICRU.

2.6. Water phantom modelling

EGSnrc/DOSXYZnrc [40] was used to model a water phantom in which dose calculations for all beam setups were calculated. PHSP2 files produced in BEAMnrc at Z = 95 cm was used as source, whereas the distance of each PHSP2 file from the isocentre was set to 5 cm. The phantom voxel sizes were adjusted depending on whether PDDs, OAPs or ROFs were simulated. In this manner, 2 mm × 2 mm × 2 mm voxels were constructed along the axis and/or plane of interest (vertical or horizontal), which reduces the amount of histories required for 1% variance. Air was introduced between the exit plane and the surface of the water phantom for 100 cm SSD setups.

2.7. Measurements

All electron data were collected according to the recommendations of the AAPM Task Group no. 106 [41]. Measurements were performed in a three-dimensional dosimetry scanning system (Blue Phantom, IBA dosimetry, Bartlett, TN) which includes a CU500E electrometer. For electron PDD data, a plane parallel chamber (Roos® Chamber Type 34001, PTW, Freiburg, Germany) with a nominal sensitive volume of 0.35 cm^3 (7.8 mm radius, 2 mm depth, water equivalent thickness of 1.3 mm and guard ring width of 4 mm) was used. OAPs were measured using a CC13 (IBA Dosimetry, Bartlett, TN) chamber with a sensitive volume of 0.13 cm^3 (air cavity diameter of 6.0 mm and length of 5.8 mm). Another CC13 chamber was used as the reference detector. OAPs and PDDs for the 2 × 2 cm^2, 3 × 3 cm^2 and 4 cm circular fields

were measured using a CC01 ionization chamber (IBA Dosimetry, Bartlett, TN) with a sensitive volume of 0.01 cm^3 (air cavity diameter of 2.0 mm and length of 3.6 mm). OmniPro™ Accept (version 6.5A, IBA Dosimetry GmbH, Schwarzenbruck, Germany) was used to control the scanning dosimetry system and to analyse scanned data. ROFs were measured at the depth of maximum dose for each respective energy-field-SSD combination, administering 100 monitor units per setup.

3. Results

3.1. Focal spot: Influence on down-stream electron energy spectra, CAX PDD and OAPs

On the left side of Fig. 4 the energy spectrum at $Z = 0$ cm (for a 0.15 mm FWHM) is given, as well as the energy spectra at $Z = 95$ cm for FWHM from 0.5 mm to 10 mm. The right side of Fig. 4 illustrates a plot of the difference between the different spectra at $Z = 95$ cm, with the 1.5 mm FWHM spectrum chosen as the reference spectrum. The largest differences occurred at the area of the most probable energy where large gradients exist, whereas noticeable changes occurred in the lower energy tail with an increase in FWHM beyond 3.0 mm. This definitive change in the energy spectrum due to a change in the focal spot FWHM correlates with the dose discrepancies observed in the CAX PDD in Fig. 5.

Fig. 5 shows the influence of a change in the FWHM on a 4 MeV CAX PDD. The observed effects are mainly evident in the BU region. No specific trend exists between the focal spot size and the variations observed in the BU. With a change in the FWHM from 0.5 mm to 10.0 mm, the % change in the dose at 1 mm depth (D_{1mm}) varied by 6.979% (min = 76.791%, max = 83.770%) relative to the maximum dose. Compared to the measured CAX PDD, focal spot sizes of 0.5 mm, 1.5 mm, 3.0 mm, 4.0 mm, 5.0 mm and 10.0 mm underestimated the BU region with doses ranging from 78.349% to 80.683%, while in contrast focal spot sizes of 1.0 mm, 2.0 mm, 6.0 mm and 7.0 mm overestimated the BU region and produced a D_{1mm} ranging from 81.622% to 83.765%. Focal spot sizes of 8.0 mm and 9.0 mm largely underestimated the BU region and produced the lowest D_{1mm} of 76.791% and 77.110%, respectively, with no effect on the dose beyond the maximum dose.

Fig. 6 illustrates simulated crossline (solid lines) and inline (dashed lines) OAPs for a 10 × 10 cm^2, 4 MeV electron beam for different focal spot FWHM. Focal spot FWHM sizes of 0.5 mm, 1.5 mm, 2.0 mm, 4.0 mm, 6.0 mm and 10.0 mm all produced profiles with a flatness of less than the acceptable 3%, while the rest exceeded this limit. The 0.5 mm, 3.0 mm and 7.0 mm FWHM underestimated the dose in both the shoulders and the central region, whereas the 9.0 mm FWHM overestimated the dose in both these regions. While the 8.0 mm FWHM underestimated the dose in the shoulders, the 5.0 mm FWHM overestimated the dose in the shoulders. Crossline penumbras varied by 1.0 mm between the range of FWHM, whereas inline penumbras varied by 0.71 mm. No clear trend between the variation in penumbra size for both crossline and inline profiles were observed with a change in the focal spot FWHM.

3.2. Initial energy spectra: Gaussian and Lévy

As shown on the left in Fig. 7, three Gaussian spectra (1–3) were constructed to model a 6 MeV electron beam from the linac. These initial spectra (at Z = 0 cm) had peak energies of 7.170 MeV each, maximum energies of 8.530 MeV, 8.770 MeV and 9.410 MeV, respectively, and FWHMs relative to the peak energy of 15.0%, 18.0% and 25.0%, respectively. After simulations throughout the entire linac head, the peak energies for Gaussian spectra 1–3 were 6.375 MeV, 6.425 MeV and 6.575 MeV; the maximum energies were 7.975 MeV, 8.225 MeV and 8.825 MeV; the FWHMs were 19.0%, 22.5% and 28.5% respectively.

Table 1 illustrates the difference between CAX PDD parameters for Gaussian spectra 1–3 versus the measured curve. Since all Gaussian spectra had identical peak energies, a difference of less than 0.1 mm was observed in R_{50} which was within 1.0 mm of the measured R_{50}. A noticeable effect on the CAX PDD curve when using broader Gaussian spectra entails a gentler dose gradient D_G along with a shallower R_{80}.

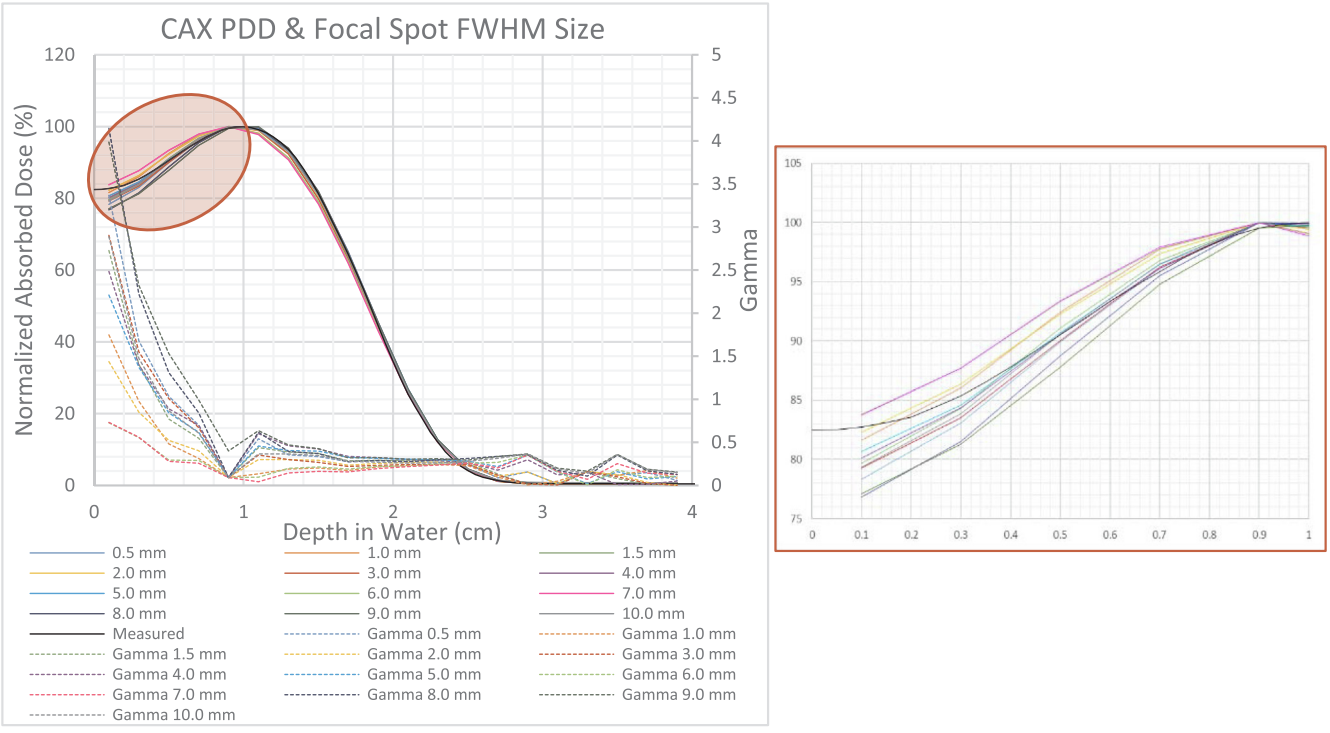

Fig 5. The effect of different focal spot sizes on a CAX PDD for a 4 MeV, 10 × 10 cm^2 electron beam in water with an SSD of 95 cm. A Gamma analysis with a 2%/2 mm dose/DTA criteria was performed on each focal spot size's corresponding CAX PDD with the measured PDD curve as the reference set. An inlay magnifies the BU region to better illustrate the dose discrepancies in the BU region.

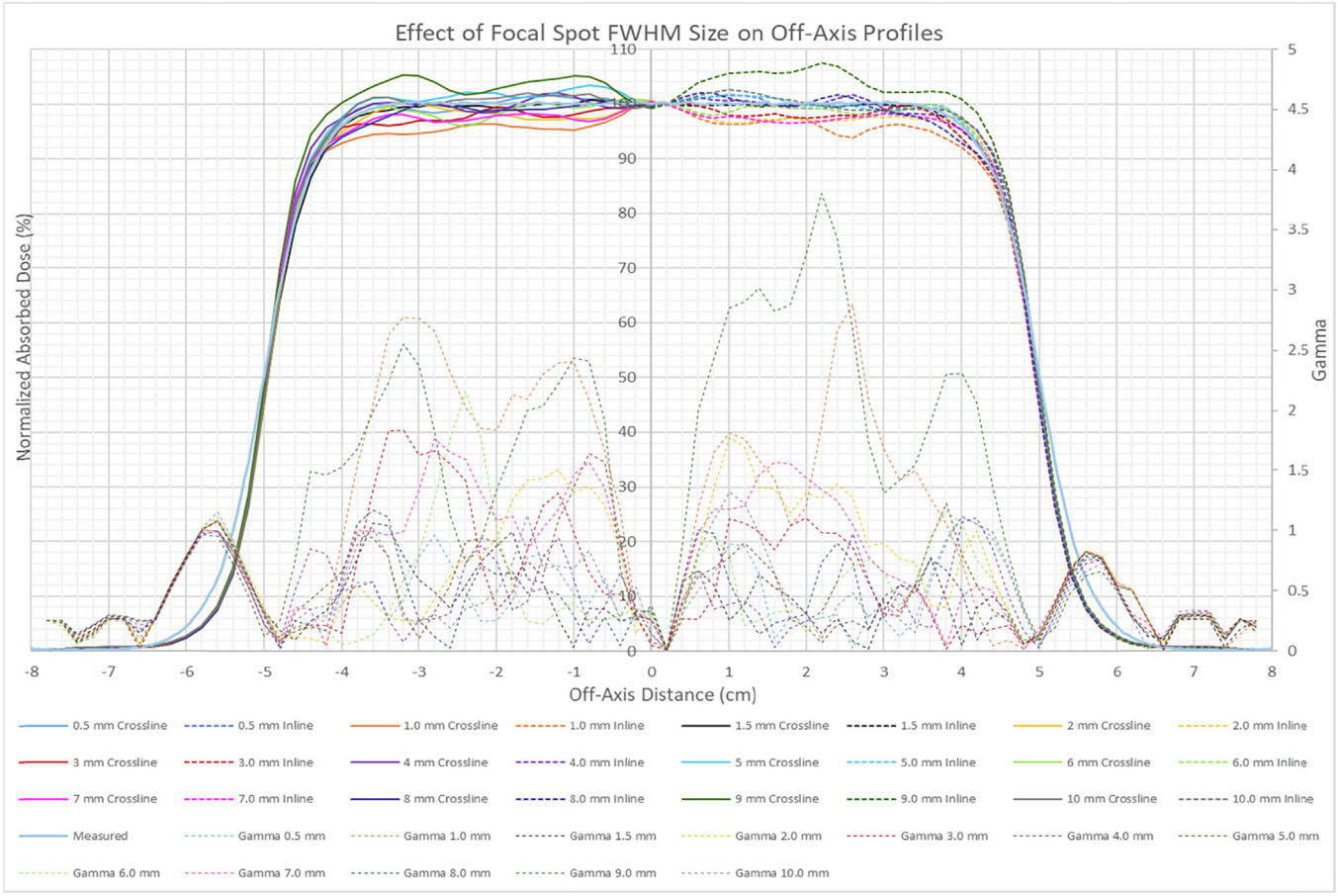

Fig 6. Crossline (left side of graph, solid lines) and Inline (right side of graph, dashed lines) OAPs for different focal spot FWHM. Profiles were extracted at the depth of maximum dose (0.90 cm) for a 4 MeV, 10 × 10 cm^2 electron beam with an SSD of 95 cm.

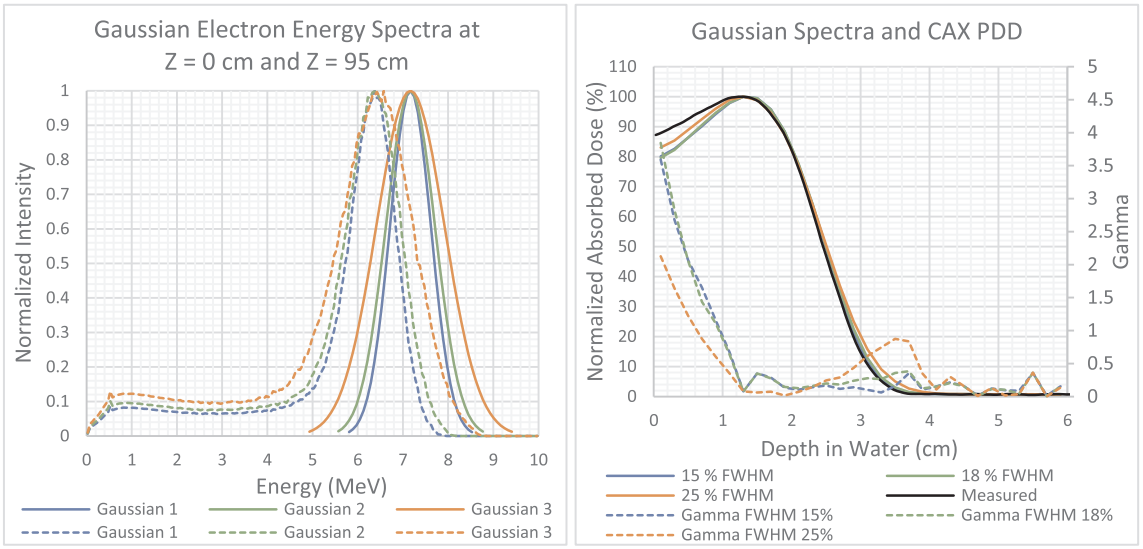

Fig 7. Left: Three 6 MeV initial Gaussian spectra, each with a peak energy of 7.170 MeV, with different FWHMs of 15.0%, 18.0% and 25.0%, represented by the solid blue (Gaussian 1), green (Gaussian 2) and orange (Gaussian 3) curves, respectively. Using these spectra as input in simulations, simulated energy spectra at Z = 95 cm were extracted from phase space files using BEAMDP and are represented by the dashed curves. Right: CAX PDDs brought about by Gaussian spectra 1–3 are shown along with a measured 6 MeV, 10 × 10 cm^2 CAX PDD at 95 cm SSD in water. Each CAX PDD curve was compared with the measured PDD curve using a Gamma analysis with a 2%/2 mm criterion.

Even though the fit to the measured CAX PDD curve beyond R_{100} is within 2%/2 mm, there exists a dose discrepancy in the $D_{1\ mm}$ of > 4% for all Gaussian spectra. This highlights the challenge when using Gaussian spectra to model the initial electron energy spectrum; that is, a lack of a single changeable parameter to only alter the dose in the BU region without significantly changing the rest of the CAX PDD curve.

The energy spectra obtained for the six different input electron spectra (Fig. 2) at Z = 95 cm are illustrated on the left in Fig. 8. The

Table 1
Comparison of CAX PDD parameters brought about by Gaussian spectra 1–3 versus a CAX PDD measurement for a 6 MeV 10 × 10 cm^2 electron beam at 95 cm SSD in water.

	$D_{1\,mm}$ (%)	R_{100} (cm)	R_{80} (cm)	R_{50} (cm)	D_G (%·cm)
Gaussian 1	80.102	1.300	2.053	2.491	−68.662
Gaussian 2	79.592	1.300	2.057	2.497	−66.987
Gaussian 3	83.055	1.300	2.042	2.507	−62.057
Measured	87.856	1.280	2.038	2.458	−69.975

most probable energy was 6.775 MeV and was virtually constant amongst all spectra. An increase in the spectrum width and lower energy tail with an increase in scaling parameter is observed, which is similar to the observations of Gaussian spectra (Fig. 7).

On the right side of Fig. 8, the effect of different scaling parameters (c_1-c_6) on a CAX PDD is illustrated. By visual inspection it is evident that there are noticeable changes on the CAX PDD curve with an increase in scaling parameter. Discrepancies in the BU region are observed along with differences in range parameters. However, the practical range and Bremsstrahlung tail seems unchanged which was expected since the maximum peak and maximum energies in the energy spectra at Z = 95 cm (Fig. 8) are nearly the same. The effect of the scaling parameter on D_{1mm}, R_{80}, R_{50} and D_g are plotted in separate graphs in Fig. 9. The variation in R_{100} for all scaling parameters was insignificant.

The variation in D_{1mm} for the range of scaling parameters investigated reached a maximum of 7.428%. Though a quadratic fit was made to data points, the variation in D_{1mm} for scaling parameters of c_1 = 0.05 to c_3 = 0.1 did not actually yield a specific trend. In a preliminary investigation, scaling parameters of 0.06, 0.07, 0.08 and 0.09 (most probable energy of 7.59 MeV at Z = 0 cm) yielded D_{1mm} values of 92.030%, 82.810%, 84.870% and 81.120%, respectively, which illustrated the same variation. The argument can therefore be made that it may not be possible to fit a trendline to the variation in D_{1mm} for different scaling parameters, since for scaling parameters < 0.1 variations in D_{1mm} are not stable.

Both R_{80} and R_{50} showed a linear decrease with an increase in scaling parameter. From the gradients produced for the linear fits to the R_{80} and R_{50} plots, a more rapid change in R_{80} with an increase in scaling parameter was observed than in R_{50}. Using these measured R_{80} and R_{50} parameters (2.12 cm and 2.56 cm, respectively) as input into the trendline equations obtained for the R_{80} and R_{50} plots, scaling parameter values of 0.045 and 0.039 were calculated. This suggests that using a scaling parameter within these bounds would produce R_{80} and R_{50} to within 0.03 mm.

The dose gradient D_g became gentler with an increase in the scaling parameter with an unclear trend in the variation in D_g for scaling parameters < 0.1. The observation here is that with an increase in scaling parameter, the decrease in R_{80} is more than the decrease in R_{20} (see Fig. 8).

3.3. CAX PDDs, OAPs and ROFs benchmarks

Simulated CAX PDDs, OAPs and ROFs at both SSDs along with Gamma analyses are supplied in the supplementary data (Supplementary figures 2–6). Following a fine tuning of the Lévy spectrum for each electron energy, simulated PDD curves complied with measured PDD curves with a 100% pass rate using a 2%/2 mm criterion for all energies, fields and SSDs. OAPs at both SSDs were simulated with a pass rate of nearly 100% using a 2%/2 mm criterion, where failed points were attributed to simulation noise in regions of low dose gradients. Noticeable from both the results at both SSDs is the overall improved fit of smaller fields. The absolute difference between measured and simulated cone factors was on average 1.468 ± 0.9% (max = 2.858%) at an SSD of 95 cm, whereas at 100 cm SSD this was 1.296 ± 0.827% (max = 2.764%). Cut-out factors at 95 cm SSD were simulated within an average absolute difference of 1.420 ± 0.707% (max = 2.560%) of measured factors, whereas at 100 cm SSD this was 1.685 ± 0.503% (max = 2.736%).

4. Discussion

The dose discrepancies observed on the CAX PDD caused by the focal spot FWHM size, as well as the dose discrepancies in the central and shoulder regions of profiles contradicts the findings by Rodrigues et al. [21] and Schreiber et al. [22]. The change in D_{1mm}varied by 6.979% with some discrepancies in the start of the build-down region. Furthermore, the flatness of simulated profiles varied from a minimum of 1.600% to 4.780%, which supports the sensitivity of the central region to a FWHM change. In agreement to the findings by Schreiber et al. [22], the changes brought about by different FWHM did not follow a specific trend with different FWHM as well as with an increasing electron energy. The choice of the FWHM was ultimately made by eliminating those FWHM that did not comply with flatness and

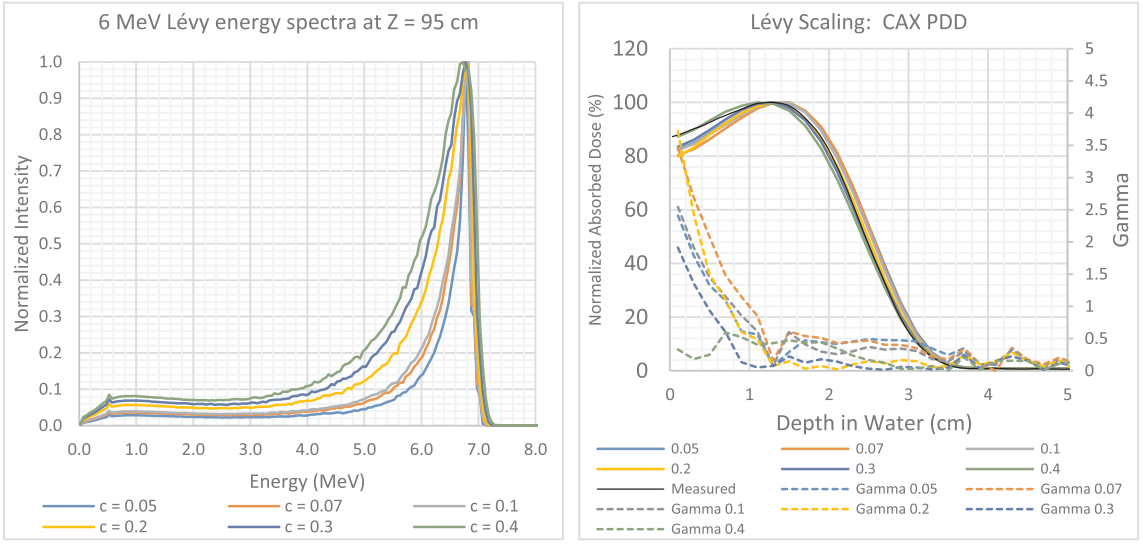

Fig 8. 6 MeV Lévy energy spectra. Left: The energy spectra at Z = 95 cm for scaling parameters from 0.05 to 0.4, obtained using BEAMDP; Right: The effect of different scaling parameters (c_1- c_6) on the CAX PDD at the depth of maximum dose (1.4 cm) as simulated in water for a 10 × 10 cm^2 6 MeV beam at 95 cm SSD. CAX PDDs were compared with the measured PDD using a Gamma analysis with a criterion of 2%/2 mm.

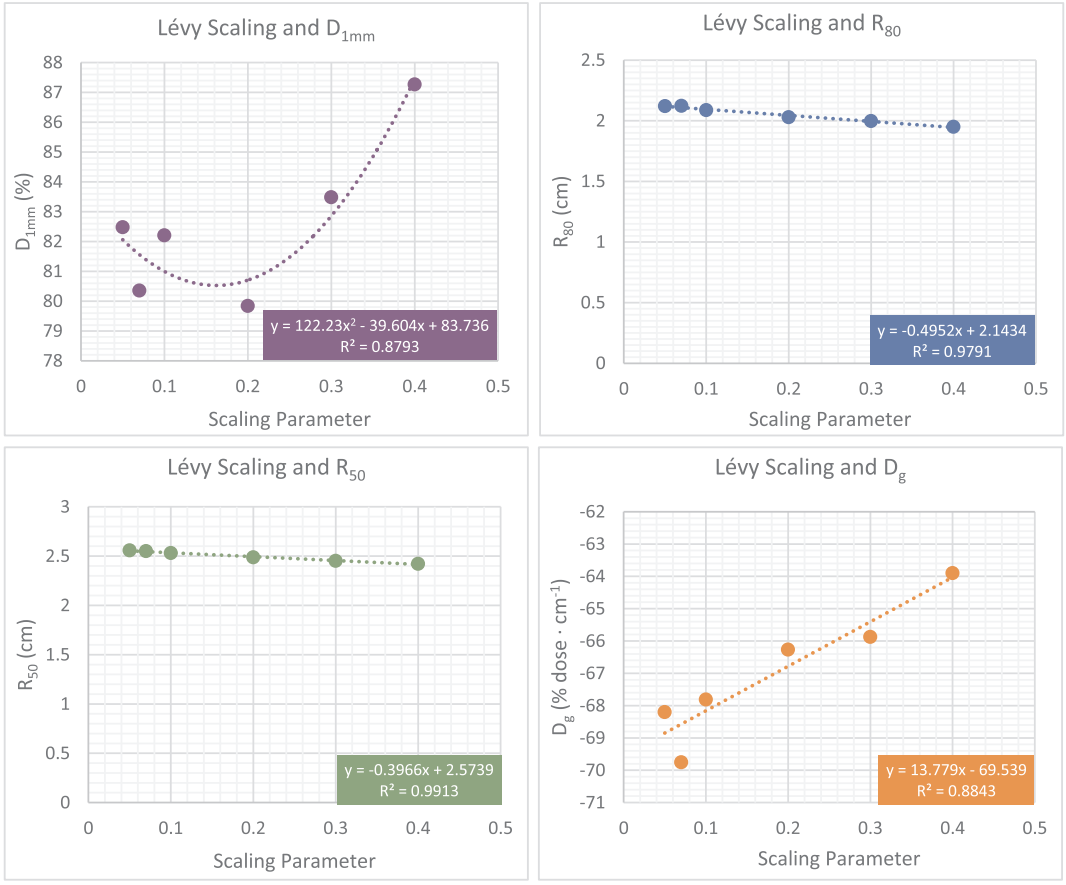

Fig 9. Plots of the observed PDD parameters $D_{1\,mm}$ (top left), R_{80} (top right), R_{50} (bottom left) and D_g (bottom right) versus different scaling parameters. Trendlines have been fitted to data with trendline equations and regression constants indicated on each graph.

penumbra width specifications. A focal spot size of 1.5 mm–2.0 mm was the obvious choice, and therefore a fixed value of 1.5 mm was chosen for all electron nominal energies. An energy dependence on the focal spot size was ruled out by a preliminary study which produced similar results for a 15 MeV model. This supports the findings by Björk et al. [19] who reported the focal spot FWHM to be between 1 mm − 2 mm for Elekta linacs.

The Gaussian spectra investigated showed that even though a match within 2%/2 mm was attainable beyond R_{100} on the CAX PDD, dose discrepancies > 4% still exists in the BU region. Matching the dose in the BU region without changing the dose in the rest of the PDD becomes a problem when using a Gaussian spectrum. This was the main motivation for the investigation of the Lévy energy spectrum, which truncates higher electron energies and considers lower electron energies in contrast to a Gaussian spectrum. An increase in the scaling parameter gives rise to a broader distribution towards the lower energy side, increases the lower-energy tail of the spectrum as well as decreases the most probable energy with a small amount. Though the adjustment of the Lévy scaling parameter with 0.1 increments can have very significant effects on the PDD curve as a whole, making fine adjustments to the scaling parameter between 0.05 and 0.1 has proven to solve the dose discrepancies observed in the BU region without significantly altering the dose beyond the depth of maximum dose. Choosing the most appropriate scaling parameter is based on a method of trial-and-error where simulations with different scaling parameters are performed simultaneously to yield the most appropriate scaling parameter. A scaling parameter of between 0.05 and 0.07 was selected for all the electron models.

The accuracy of the electron model was evident in the PDD, OAP and ROF results (see Supplementary figures 2–6) which indicated that the model complied with the 2%/2 mm criterion. This was not only attributed to the success of the Lévy energy spectrum, but the contribution of the skin_depth_for_BCA parameter should be mentioned. Increasing this parameter from 3 to 50 mean free paths effectively forces single scattering mode to occur further away from boundaries and hence smaller fields are handled more sensitively. This is evident in the small field OAPs and supports one of the findings of Mihaljevic et al. [39].

5. Conclusions

Benchmarking of clinical electron fields with stringent Gamma criteria requires detailed and accurate modelling of both the linac head components as well as the initial electron beam properties. Accurate modelling of unknown initial electron beam properties plays a critical role in the success of the developed model. The focal spot size could be determined iteratively from simulations, where the chosen FWHM value corroborated with the findings of published studies. The Lévy energy spectrum not only better characterized the initial energy spectrum of the electron beam as it exits the waveguide-bending magnet system of the linac, but also provided a valuable free parameter which by fine adjustment could improve the match of dose in the BU region of CAX PDDs without significantly altering the PDD curve beyond the depth of maximum dose. This is a major benefit above Gaussian spectra which do not offer such a parameter. Performing a small subset of simulations provided the choice of scaling parameter for each electron nominal energy.

The developed full electron model complied in its aim to simulate CAX PDDs and OAPs with a 100% pass rate using a 2%/2 mm Gamma criterion, and ROFs were simulated to within 3% of measured cone and

cut-out factors. The model could therefore be further utilized in the development of modulated electron radiotherapy.

Declaration of Competing Interest

The authors declare that they have no known competing financial interests or personal relationships that could have appeared to influence the work reported in this paper.

Acknowledgements

This research project was funded by the South African Medical Research Council (MRC) with funds from National Treasury under its Economic Competitiveness and Support Package. Research and any publication thereof is the result of funding provided by the Medical Research Council of South Africa in terms of the MRC's Flagship Awards Project [SAMRC-RFA-UFSP-01-2013/HARD].

Appendix A. Supplementary data

Supplementary data to this article can be found online at https://doi.org/10.1016/j.ejmp.2019.09.073.

References

[1] Khan FM, Gibbons JP, Sperduto PW. Khan's Treatment Planning in Radiation Oncology. fourth ed. Netherlands: Wolters Kluwer; 2016.
[2] D. Mihailidis, Therapeutic Electron Beams: Clinical Dosimetry and AAPM TG-70.
[3] Mayles P, Nahum A, Rosenwald JC. Handbook of Radiotherapy Physics: Theory and Practice. 1st ed. Taylor & Francis; 2008.
[4] Chetty IJ, et al. Report of the AAPM Task Group No. 105: Issues associated with clinical implementation of Monte Carlo-based photon and electron external beam treatment planning. Med Phys 2007;34(12):4818–53.
[5] Jabbari N, Barati AH, Rahmatnezhad L. Multiple-source models for electron beams of a medical linear accelerator using BEAMDP computer code. Reports Pract Oncol Radiother 2012;17(4):211–9.
[6] Mohammed M, El Bardouni T, Boukhal H, Azahra M, Chakir E. Implementation of the EGSnrc / BEAMnrc Monte Carlo code – application to medical accelerator SATURNE43. Int J Innov Appl Stud 2014;6(3):635–41.
[7] Ma CM, Faddegon BA, Rogers DWO, Mackie TR. Accurate characterization of Monte Carlo calculated electron beams for radiotherapy. Med Phys 1997;24(3):401.
[8] Spezi E, Lewis G. An overview of Monte Carlo treatment planning for radiotherapy. Radiat Prot Dosim 2008:1–7.
[9] Zoubair M, El Bardouni T, El Gonnouni L, Boulaich Y, El Bakkari B, El Younoussi C. Application of variance reduction techniques in Monte Carlo simulation of clinical electron linear accelerator. Nucl Inst Methods Phys Res A 2012;661(1):93–7.
[10] D.W.O. Rogers, BEAMnrc: a code to simulate radiotherapy external beam sources, 2007, pp. 1–31.
[11] Ojala J, Hyödynmaa S, Pitkänen M. BEAMnrc Monte Carlo modelling of linear accelerator using parallel computing grid – validation of a common, fixed geometry model for photon and electron beams. Proceedings of the XVIth ICCR. 2010.
[12] Jiang SB, Kapur A, Ma C. Electron beam modeling and commissioning for Monte Carlo treatment planning. Med Phys 2000;27(1):180–91.
[13] Ali OA, Willemse CA, Shaw W, O'Reilly FHJ, du Plessis FCP. Monte Carlo electron source model validation for an Elekta Precise linac. Med Phys 2011;38(5):2366.
[14] Jabbari N, Hashemi-Malayeri B. Monte Carlo modeling of electron beams from a Neptun 10PC medical linear accelerator. Nukleonika 2009;54(4):233–8.
[15] Jabbari K, Anvar HS, Tavakoli MB, Amouheidari A. Monte Carlo Simulation of Siemens ONCOR Linear Accelerator with BEAMnrc and DOSXYZnrc Code. J Med Signals Sens 2013;3(3):172–9.
[16] Udale M. A Monte Carlo investigation of surface doses for broad electron beams. Phys Med Biol 1988;33(8):939–54.
[17] Akino Y, Zhu TC, Das IJ. Parameterization of electron beam output factor. Phys Medica 2015;31(4):420–4.
[18] Deng J, Jiang SB, Pawlicki T, Li J, Ma C-M. Derivation of electron and photon energy spectra from electron beam central axis depth dose curves. Phys Med Biol 2001;46:1429–49.
[19] Björk P, Knöös T, Nilsson P. Influence of initial electron beam parameters on Monte Carlo calculated absorbed dose distributions. Phys Med Biol 2002;47:4019–41.
[20] Faddegon BA, Kawrakow I, Kubyshin Y, Perl J, Sempau J, Urban L. Accuracy of EGSnrc, Geant4 and PENELOPE Monte Carlo systems for simulation of electron scatter in external beam radiotherapy. Phys Med Biol 2009;54(20):6151–63.
[21] Rodrigues A, Sawkey D, Yin F, Wu Q. A Monte Carlo simulation framework for electron beam dose calculations using Varian phase space files for TrueBeam Linacs. Med Phys 2015;42(5):2389–403.
[22] Schreiber EC, Faddegon BA. Sensitivity of large-field electron beams to variations in a Monte Carlo accelerator model. Phys Med Biol 2005;50(5):769–78.
[23] Maskani R, Tahmasebibirgani M, Hoseini-Ghahfarokhi M, Fatahiasl J. Determination of initial beam parameters of varian 2100 CD linac for various therapeutic electrons using PRIMO. Asian Pacific J Cancer Prev 2015;16:7795–801.
[24] Oprea M, Constantin C, Mihailescu D, Borcia C. A Monte Carlo investigation of the influence of initial electron beam CHaracteristics on the absorbed DOse distributions Obtained With a 9 MeV IORT Accelerator. UPB Sci Bull Ser A 2012;74(4).
[25] Rogers DWO, Faddegon BA, Ding GX, Ma CM, We J, Mackie TR. BEAM: a Monte Carlo code to simulate radiotherapy treatment units. Med Phys 1995;22(5):503–24.
[26] Fix MK, et al. Generalized eMC implementation for Monte Carlo dose calculation of electron beams from different machine types. Phys Med Biol 2013;58(9):2841–59.
[27] Campos LT, Braz D, Antonio L, Rosa R. Monte Carlo Simulations of Regular Fields for Electron Beams from a Medical Accelerator using EGSnrc. International Nuclear Atlantic Conference. 2009.
[28] Alexander A, Soisson E, Renaud MA, Seuntjens J. Direct aperture optimization for FLEC-based MERT and its application in mixed beam radiotherapy. Med Phys 2012;39(8):4820–31.
[29] Olsson M. Monte Carlo Simulations of the Elekta SLi Plus Electron Applicator System – A Base for A New Applicator Design to Reduce Radiation Leakage. Sweden: Lund University; 2003.
[30] Lamoureux M, Charles P. General deconvolution of thin-target and thick-target Bremsstrahlung spectra to determine electron energy distributions. Radiat Phys Chem 2006;75(10):1220–31.
[31] Mihailescu D, Borcia C. Monte Carlo simulation of the electron beams produced by a linear accelerator for intra-operative radiation therapy. Rom Reports Phys 2014;66(1):61–74.
[32] B.W.I. Kawrakow, E. Mainegra-Hing, D.W.O. Rogers, F. Tessier, The EGSnrc Code System : Monte Carlo Simulation of Electron and Photon Transport, 2011.
[33] D.W.O. Rogers, B. Walters, I. Kawrakow, BEAMnrc Users Manual, 2011.
[34] Elekta. Elekta, iCom Interface Information. West Sussex, United Kingdom: Worldwide Product Manudfacturing Center – Oncology; 2013.
[35] Huang VW, Seuntjens J, Devic S, Verhaegen F. Experimental determination of electron source parameters for accurate Monte Carlo calculation of large field electron therapy. Phys Med Biol 2005;50(5):779–86.
[36] Harris GM. Development and Validation of an Electron Monte Carlo Model for the Elekta Infinty Accelerator. Georgia Inst Technol 2012.
[37] Landau L. On the energy loss of fast particles by ionization. J Phys 1944;8(4):201–5.
[38] Nolan JP. Maximum Likelihood Estimation and Diagnostics for Stable Distributions. In: Barndorff-Nielsen OE, Resnick SI, Mikosch T, editors. Lévy Processes: Theory and Applications. Boston, MA: Birkhäuser Boston; 2001. p. 379–400.
[39] Mihaljevic J, Soukup M, Dohm O, Alber M. Monte Carlo simulation of small electron fields collimated by the integrated photon MLC. Phys Med Biol 2011;56(3):829–43.
[40] B. Walters, I. Kawrakow, D.W.O. Rogers, DOSXYZnrc Users Manual, 2011.
[41] Das IJ, et al. Accelerator beam data commissioning equipment and procedures: report of the TG-106 of the Therapy Physics Committee of the AAPM. Med Phys 2008;35(9):4186–215.